Stochastic joint inversion of temperature and self-potential data

Abderrahim Jardani, A. Revil

Geophys. J. Int. (2009) **179,** 640–654 doi: 10.1111/j.1365-246X.2009.04295.x

Stochastic joint inversion of temperature and self-potential data

A. Jardani[1] and A. Revil[1,2]

[1] *Colorado School of Mines, Dept. of Geophysics, Golden, CO, USA. E-mail: arevil@mines.edu*
[2] *INSU-CNRS LGIT UMR* 5559*, Université de Savoie, Equipe Volcans, Le Bourget du Lac, France*

Accepted 2009 June 12. Received 2009 June 12; in original form 2009 February 1

SUMMARY

The flow of the ground water is responsible for both thermal and self-potential anomalies. Temperature is usually recorded in boreholes while self-potential is usually recorded at the ground surface of the Earth. This makes the joint inversion of temperature and self-potential data together an attractive approach to invert permeability. We use an Adaptive Metropolis Algorithm to determine the posterior probability densities of the material properties of different geological formations and faults by inverting jointly self-potential and temperature data. The algorithm is tested using a synthetic case corresponding to a series of sedimentary layers overlying a low-permeability granitic substratum. The flow of the ground water (computed in steady-state condition) is mainly localized in two faults acting as preferential fluid flow pathways. The first fault is discharging warmed ground water near the ground surface while the second fault acts as a recharge zone of cold water (a classical scenario in geothermal systems). The joint inversion algorithm yield accurate estimate of the permeability of the different units only if both temperature and self-potential data are jointly inverted. An application using real data is also performed. It concerns the upwelling of a hydrothermal plume through a set of faults and permeable formations at the Cerro Prieto geothermal field in Baja California. The optimized permeabilities are in close agreement with independent hydrogeological estimates.

Key words: Electrical properties; Hydrothermal systems; Permeability and porosity; Heat generation and transport.

1 INTRODUCTION

The traditional way to infer ground water flow is by making *in situ* measurements of the hydraulic heads in a set of piezometers or by using chemical tracers (Fetter 1994). Unfortunately, these *in situ* measurements are often expensive and the spatio-temporal quality of the information is strongly dependent on the number of available wells. To avoid these problems, several geophysical methods have been developed to determine non-intrusively some information related to the flow of the ground water or the permeability distribution. Ground penetrating radar, DC and EM-based electrical resistivity tomography, nuclear magnetic resonance, and seismic methods are among the most popular methods used in hydrogeophysics for that purpose. These methods have the advantage of being non-invasive and sensitive, to some extent, to the distribution of the water content of the ground. However, it is generally recognized that these methods are difficult to use to determine the permeability distribution. Our goal is to develop a new methodology to characterize the distribution of the permeability of geological units using passive methods that are directly sensitive to ground water flow. Two types of data honour these constraints: the self-potential method and temperature measurements.

The self-potential method corresponds to the passive measurements of the electrical field at the ground surface of the Earth or possibly in boreholes. The source of the electrical field corresponds to the existence of *in situ* currents. These currents can be due to ground water flow (Corwin & Hoover 1979; Lachassagne & Aubert 1989; Revil & Pezard 1998; Rizzo *et al.* 2004; Rozycki *et al.* 2006), gradients of the chemical potential of the ionic species (Revil & Linde 2006), temperature (Revil 1999), and redox potential (Stoll *et al.* 1995; Revil *et al.* 2001; Castermant *et al.* 2008). The second and third contributions can be modelled using mechanistic models (Revil & Linde 2006) and are known to be generally very small with respect to the first and fourth contributions. The electro-redox contribution can be separated from the contribution related to ground water flow (see Rizzo *et al.* 2004; Arora *et al.* 2007, for two distinct examples). This let us with the contribution associated with ground water flow. For example, Suski *et al.* (2006) was able to validate the physics of the streaming potential in the field though an infiltration experiment in which all the material properties were independently measured. Jardani *et al.* (2006, 2007, 2008) have recently developed several algorithms based on Tikhonov regularization to map the pattern of ground water flow using self-potential measurements and electrical resistance tomograms.

Temperature is also a tracer of ground water flow. In absence of ground water flow, there is a natural vertical thermal gradient in the ground called the reference geothermal gradient. This reference geothermal gradient depends on the heat flux of the Earth and the distribution of the thermal conductivity of rocks. The flow of ground water carries a net amount of heat that disturbs the geothermal

gradient (Bredehoeft & Papadopulos 1965). Temperature measurements have been used to determine the pattern of the vertical component of the ground water flow (Andrews & Anderson 1979; Smith & Chapman 1983; Tabbagh *et al.* 1999; Cheviron *et al.* 2005).

In the past, self-potential and temperature data have been considered independently to estimate the pattern of ground water flow or alternatively the permeability distribution. The question is therefore to know if these data taken together offer complementary information on the distribution of the permeability. We demonstrate in this paper that this is indeed the case. To our knowledge, this is the first time that an algorithm is proposed to invert jointly self-potential and temperature data. Our goal is to estimate the transport properties of aquifers or the intrinsic permeability of permeable pathways like fault zones in geothermal systems. High-permeability pathways are required to bring hydrothermal water to the ground surface (Forster & Smith 1988) and in most geothermal system the low vertical permeability of rocks implies that faults are conduits for hydrothermal fluids. However, as hydrothermal fluids migrate from depth, they cool down. This leads to significant mineral precipitations, which reduce the permeability and ultimately block discharge in the absence of any physical mechanism of permeability maintenance like deformation associated with changes in the stress tensor (Bishop & Bird 1987; Revil & Cathles 2002). The problems related to the determination of the material properties from geophysical data like self-potential and temperature data are (1) the non-linearity of the inverse problem and (2) the potential non-uniqueness of the distribution of the values of the material properties that satisfy to the constraints of geophysical data and *in situ* observations. The non-linear character of the inverse problem can be responsible for the existence of secondary minima in the cost function to minimize (Mosegaard & Sambridge 2002; Sambridge & Mosegaard 2002; Tarantola 2005). To circumvent these difficulties, a variant of the 'Markov Chain Monte Carlo' (MCMC) methods called the Adaptive Metropolis Algorithm (AMA; Haario *et al.* 2001, 2004) is used in this study.

2 THEORETICAL BACKGROUND

2.1 Field equations

We consider below steady state conditions, no source or sink terms for water, and an incompressible pore fluid. With these assumptions, the continuity equation for the flow of the ground water is $\nabla \cdot \mathbf{u} = 0$ where the seepage velocity $\mathbf{u}$ (in m s^{-1}) obeys the Darcy constitutive equation $\mathbf{u} = -K\nabla H$, K is the hydraulic conductivity (in m s^{-1}) and H the hydraulic head (in m). The distribution of the pressure head is therefore obtained by solving a Poisson-type PDE using boundary conditions and the distribution of the hydraulic conductivity. The relationship between the hydraulic conductivity and the permeability k (in m^2) is $K = k\rho_{\mathrm{w}}g/\eta_{\mathrm{w}}$, where η_{w} and ρ_{w} are the dynamic viscosity (in Pa s) and the mass density of the pore water (kg m^{-3}), respectively and g is the acceleration of the gravity (m s^{-2}). The viscosity and the mass density of the pore fluid are dependent on the temperature. In the following study, we use first-order linear relationships to account for temperature. Typically, the permeability of rocks can vary over 11 orders of magnitude and is a strongly scale-dependent property. This is why estimating the permeability at large scale is an important issue in Earth Sciences.

In our model, the self-potential response is related to ground water flow through an electrokinetic coupling mechanism. The self-potential φ (in V) is governed by a Poisson equation (e.g. Jardani *et al.* 2008),

$$\nabla \cdot (\sigma \nabla \varphi) = \nabla \cdot \left(\bar{Q}_V \mathbf{u}\right), \tag{1}$$

where σ (in S m^{-1}) is the electrical conductivity of the porous material. The right-hand side of eq. (1) corresponds to the source term associated with the Darcy velocity distribution and the heterogeneity in the distribution of the volumetric charge density $\bar{Q}_V$ (expressed in C m^{-3}). The volumetric charge density $\bar{Q}_V$ is the effective charge density occurring in the pore space of the porous material because of the electrical double layer at the mineral/water interface (Leroy *et al.* 2007, 2008; Jougnot *et al.* 2009). The relationship between this volumetric charge density and the more classical streaming potential coupling coefficient C (in V Pa^{-1}) has been investigated by Revil *et al.* (2005), Linde *et al.* (2007), Bolève *et al.* (2007) and Crespy *et al.* (2008). They found that $C = -\bar{Q}_V\, k/\sigma$ where k and σ have been defined above. For example, for an intact Inada granite sample, Tosha *et al.* (2003) measured $C = -0.02 \times 10^{-6}$ V Pa^{-1}, $k = 9 \times 10^{-19}$ m^2 and $\sigma = 0.008$ S m^{-1} (pore fluid: 0.1 M KCl). This yields $\bar{Q}_V = 2 \times 10^8$ C m^{-3}.

The self-potential distribution is therefore obtained by solving first the boundary-value problem for the hydraulic head. The solution is then used to determine the seepage velocity distribution using the distribution of the hydraulic conductivity. Knowing the distribution of the excess of electrical charge per unit volume, the source term of the Poisson equation can be obtained and the Poisson equation can be solved with appropriate boundary conditions.

In our modelling, the ground surface is considered to be an insulating boundary and therefore the normal component of the current density vanishes at this boundary ($\hat{\mathbf{n}} \cdot \nabla\varphi = 0$, where $\hat{\mathbf{n}}$ is the unit vector normal to the ground surface). An important point is that the electrical potential is never measured in an absolute sense at the ground surface of the Earth. It is measured relatively to a self-potential station called the 'reference station'. This peculiarity of the self-potential data should be considered both in the forward and inverse numerical modelling (see Jardani *et al.* 2008 for details).

In steady-state condition, the heat flow equation is given by (Tabbagh *et al.* 1999),

$$\nabla \cdot (\lambda \nabla T) = \nabla \cdot (\rho_{\mathrm{w}} C_{\mathrm{w}} T \mathbf{u}), \tag{2}$$

where T is the average temperature of the porous medium (in K) and λ (in W m^{-1} K^{-1}) is the thermal conductivity of the porous material, C_{w} (in J kg^{-1} K^{-1}) is the heat capacity of the pore water per unit mass, respectively. For water saturated porous rocks, the thermal conductivity varies typically inside one order of magnitude. Note that eq. (2) is similar to eq. (1) and the two source terms of these equations are controlled by the seepage velocity $\mathbf{u}$. However, the source term of eq. (2) is temperature dependent so this PDE is non-linear. Because the pore fluid viscosity and density entering the hydraulic problem are temperature dependent, the hydraulic and the thermal problems are coupled. The hydraulic and self-potential equations are semi-coupled because the electro-osmotic effect (i.e. the feedback coupling between the electrical field and the flow) is negligible (see Revil *et al.* 1999, for details).

2.2 Relationships between the material properties

So far, we have said nothing between the relationships that can be used to connect the material properties entering the hydraulic, electrical, and thermal problems described above. The hydraulic problem, in steady-state condition, is controlled only by the distribution of the hydraulic conductivity K. The self-potential problem

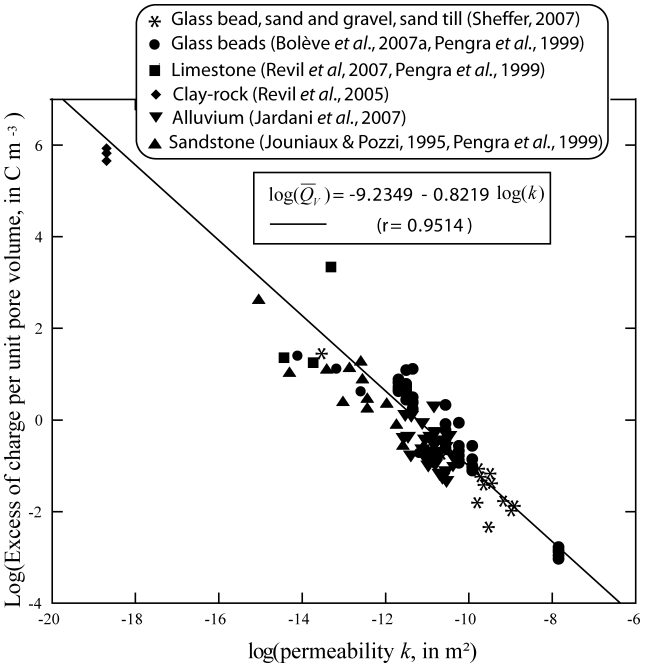

Figure 1. Bulk charge density of the diffuse layer per unit pore volume of the rock as a function of the permeability k. The experimental data are from different types of rocks and the pH of the electrolytes is comprised between 6 and 9. Experimental data from Jouniaux & Pozzi (1995), Pengra *et al.* (1999), Revil *et al.* (2005), Bolève *et al.* (2007), Revil *et al.* (2007), Sheffer (2007) and Jardani *et al.* (2007).

is controlled by the distribution of the electrical conductivity σ, the distribution of the charge density per unit pore volume $\bar{Q}_V$, and the distribution of the seepage velocity. The thermal problem, in steady-state conditions, is controlled by the distribution of the thermal conductivity λ and the distribution of the seepage velocity. It is legitimate to wonder if the material properties entering the field equations are entirely independent or if they are correlated in the field and if yes what is the degree of these correlations. Are these relationships truly useful to establish prior constraints in an inverse model?

In Fig. 1, we plot various experimental data to look at the relationship between the excess of charge per unit pore volume and the permeability. In Fig. 1, we used published data from a variety of rock types. We observe a strong relationship described by,

$$\log_{10} \bar{Q}_V = -9.2 - 0.82 \log_{10} k, \tag{3}$$

where $\bar{Q}_V$ is expressed in C m^{-3} and k is expressed in m^2. The scatter shown in their plot corresponds mainly to the fact that the measurements are performed for various physicochemical conditions of pH, mineralization and composition of the pore water. The strong connection between these two parameters holds because they are both strongly dependent on the specific surface area of the porous rocks and sediments.

The pore-scale problems defining the permeability, the electrical conductivity, and the thermal conductivity share some common characteristics (e.g. Brace 1977; Bernabé & Revil 1995; Friedman & Seaton 1998; Revil 2000; Revil *et al.* 2002) and therefore these material properties can exhibit some degree of correlation in the field. There are no universal laws to formulate some simple, yet general, relationships between these three properties. Experimental data and borehole measurements show that such universal relationships are unlikely to exist. In this study, we take the conservative assumption that these three petrophysical properties are independent. Note however that the approach we follow below is flexible and could be used to incorporate statistical relationships between material properties for a specific environment. These statistical relationships can be field-dependent and be derived for instance from borehole data in existing wells using a coded lithological description.

3 FORWARD MODELLING AND SENSITIVITY ANALYSIS

3.1 Forward modelling

The goal of the present section is to understand the self-potential and temperature signatures of ground water flow. We are especially interested to understand the sensitivity of these signatures to the values of the material properties entering the PDE (Poisson equations) to solve, our end-goal being the inversion of permeability. We perform therefore a sensitivity analysis of the three material properties entering the system of equations described in Section 2 upon the self-potential and temperature signatures of ground water flow. In steady-state conditions, the material properties of interest are the permeability k, the electrical conductivity σ, and the thermal conductivity λ of each 'unit' of a geological system. A 'unit' can be a sedimentary layer, the basement or a fault for instance.

The synthetic model considered in this paper is similar to the synthetic model investigated numerically by Rath *et al.* (2006) for comparison (see Fig. 2a). This model is used because it shows a reasonable degree of geological complexity that is similar to real case studies. The synthetic model comprises 7 units. Each unit is characterized by a value of the permeability k, a value of the electrical conductivity σ, and a value of the thermal conductivity λ. The 'true' values are reported in Table 1. The substratum is the less permeable unit while the two fault zones are the most permeable pathways of the system. The geometry of the system is assumed to be deterministically known (from seismic data for instance). In the following, we will consider arbitrarily that the properties of the two faults are the same.

To solve the forward problem, we need to specify the values of the material properties and to impose boundary conditions for the temperature (or for the heat flux), the hydraulic head (or the Darcy velocity), and the (self-)potential (or the current density). We first solve the hydraulic problem by imposing the following boundary conditions at the top surface of the system for the hydraulic head: $H = -0.01125\, x + 5920$ m for $x \in [0$ m, 2680 m$]$, $H = 5900$ m for $x \in [2680$ m, 2920 m$]$, $H = 0.005\, x + 5884$ m for $x \in [2920$ m, 11000 m$]$. These boundary conditions are used to simulate a topography of the water table. We also impose the hydraulic heads (above hydrostatic levels) along the left- and right-hand boundaries of the system in agreement with the value given at the top boundary and hydrostatic trends. The side and bottom boundaries are considered to be impervious.

The resolution of the hydraulic problem is used to infer the distribution of the Darcy velocity $\mathbf{u}$. This distribution can be used in turn to compute the source current density $\mathbf{j}_S = \bar{Q}_V \mathbf{u}$ where $\bar{Q}_V$ is the charge per unit volume of a given formation (see Section 2). We use eq. (3) in a deterministic way. The divergence of the source current density corresponds to the source term used to determine the distribution of the self-potential φ, see eq. (1). We impose $\varphi = 0$ at all the boundaries except at the ground surface, which corresponds to an insulating boundary with air ($\mathbf{n} \cdot \nabla\varphi = 0$ where

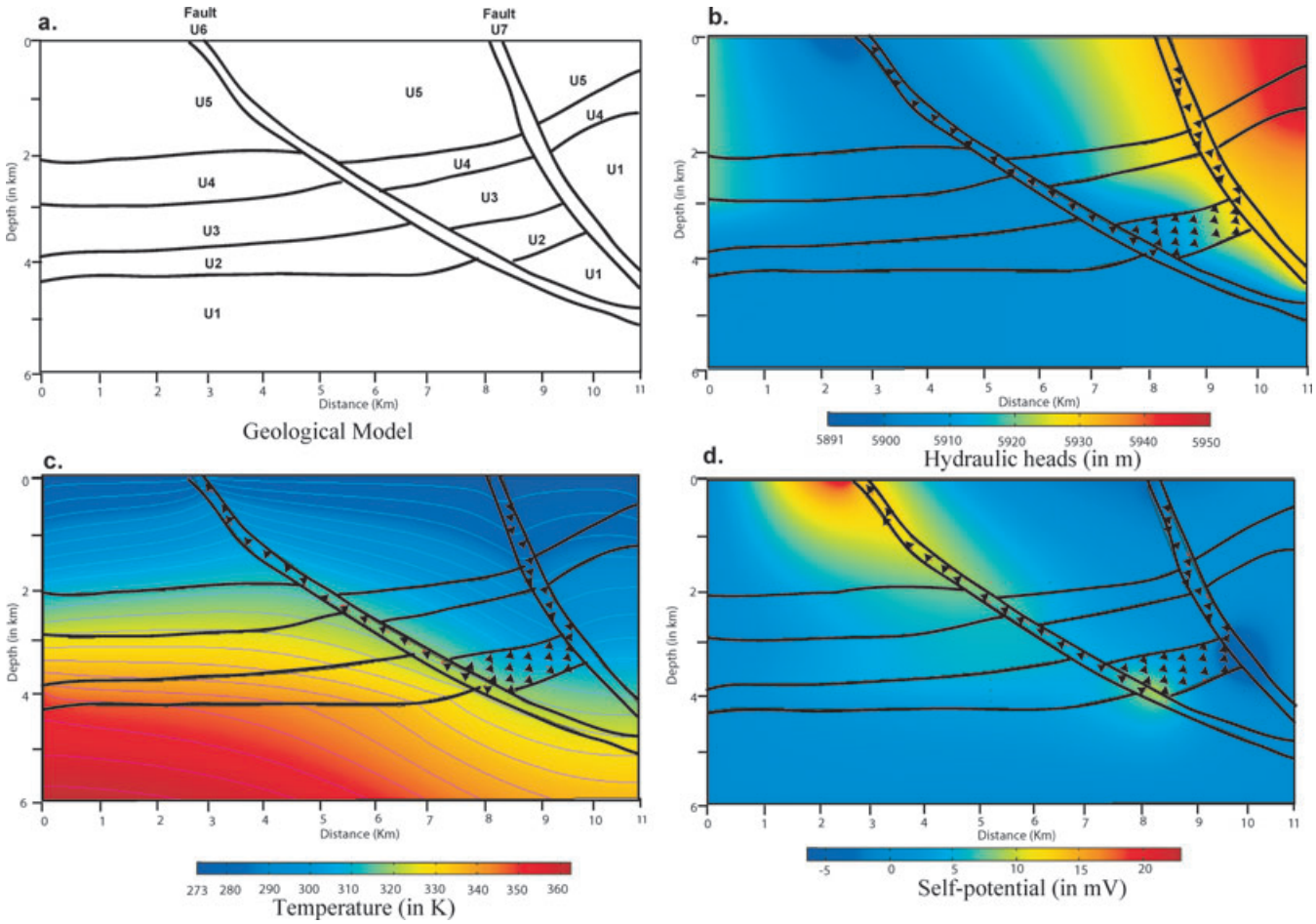

Figure 2. Sketch of the synthetic model and forward numerical simulations. (a) The synthetic model comprises seven hydraulic units (including two faults U6 and U7). The material properties of the different formations materials are reported in Table 1. (b) Distribution of the hydraulic heads. The arrows represent the direction of the Darcy velocity (the true magnitudes are smaller in Unit U2 where the flow is more pervasive, than in the fault planes). (c) Distribution of the temperature in steady-state condition of ground water flow. (d) Distribution of the self-potential associated with the ground water flow pattern.

Table 1. Material properties used for the synthetic model. U6 and U7 correspond to the faults. U1 corresponds to the granitic basement, U2 to a carbonate, U3 to a shale, U4 and U5 to clayey sandstones.

Unit	k (in m^2)	σ in S m^{-1})	λ (in W m^{-1} K^{-1})	Log($\bar{Q}_V$) (in C m^{-3})
U1	1×10^{-20}	1×10^{-3}	6	7.2
U2	1×10^{-14}	2×10^{-3}	2.5	2.3
U3	1×10^{-19}	1×10^{-1}	3	6.4
U4	1×10^{-16}	2×10^{-2}	3	3.9
U5	1×10^{-16}	1×10^{-2}	2.5	3.9
U6	5×10^{-13}	1×10^{-2}	4	0.87
U7	5×10^{-13}	1×10^{-2}	4	0.87

n is the unit vector normal to the ground surface). Such a boundary conditions should be examined carefully for a real case study (as shown in Section 5). Usually, it is better to use a padded mesh so this boundary condition applies far enough from the primary and secondary self-potential sources in the investigated system.

All the self-potential values need to be referenced to a specific point (called the reference) like in a real experiment (see Suski *et al.* 2006; Jardani *et al.* 2008). In our case, the reference station $\varphi = 0$ is chosen arbitrarily at the position Ref($x = 6000$ m, $z = 0$ m) located at the ground surface in the middle of the profile. This choice has no effect on the results as long as we keep in mind where this reference is located.

As shown in Section 2, we use the distribution of the Darcy velocity to compute also the distribution of the advective heat flux $\mathbf{h}_S = \rho_w C_w T \mathbf{u}$ (in W m^{-2}). For the thermal boundary conditions, we use a constant temperature ($T_0 = 273$ K) at the ground surface and we impose the heat flux (60 mW m^{-2}) at the bottom boundary of the system. This generates a low temperature gradient of approximately 15 °C km^{-1}.

The partial differential equations discussed in Section 2 are solved with the finite element code 'Comsol Multiphysics 3.4' with a fine triangular meshing. Regarding the mesh, we performed various tests to get a mesh-independent result. The code was also benchmarked against analytical solutions for the ground water flow and thermal problems. The resulting distributions of the hydraulic heads, the self-potential data, and the temperature data are shown in Figs 2(b)–(d).

The fault U7 on the right-hand side of the Fig. 3 creates a recharge zone because of its high hydraulic transmissivity and the boundary condition for the hydraulic head at the top surface of the system. At the opposite, the fault U6 is discharging hot water near the ground surface (see Fig. 2b). These two areas are connected by the permeable unit U2 (see Fig. 2b). Such a ground water flow pattern is quite common (see Revil & Pezard 1998 for instance).

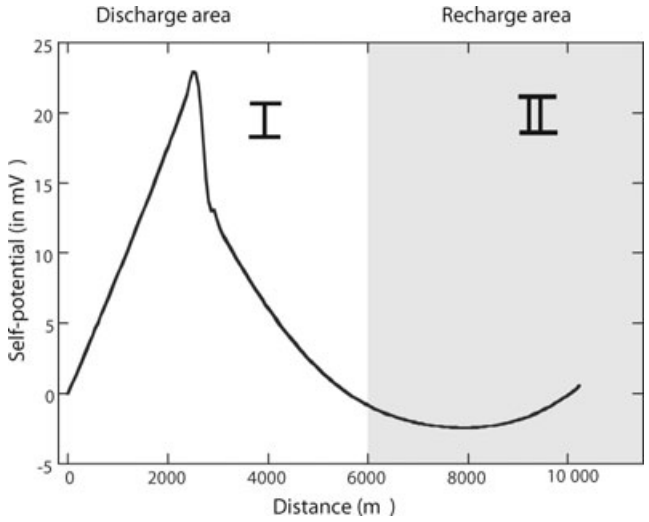

Figure 3. Distribution of the self-potential (in mV) at the ground surface in steady-state conditions. The signature of the discharge area (Zone I) corresponds to a positive self-potential anomaly (with respect to the potential at the position of the reference electrode located at $x = 6000$ m, $z = 0$). The self-potential signature of the recharge area (Zone II) corresponds to a negative self-potential anomaly with respect to the position of the reference.

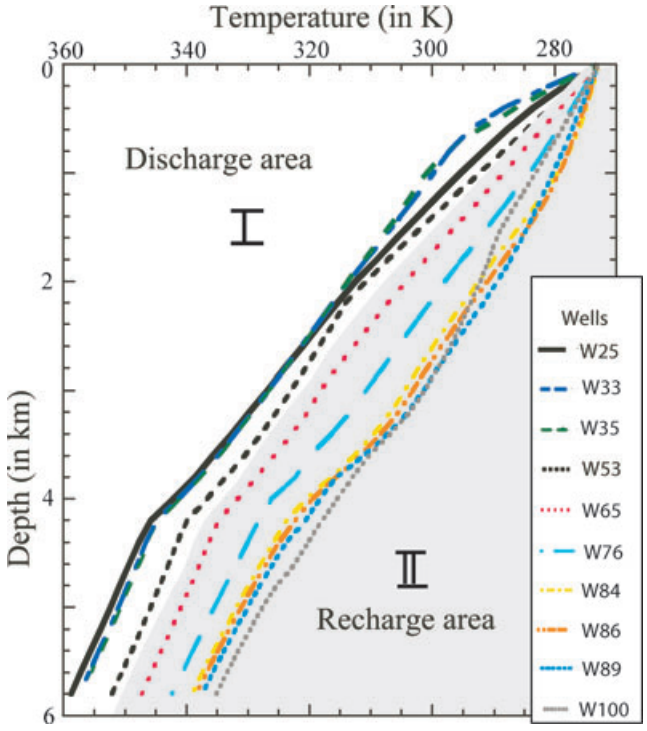

Figure 4. Temperature profiles along different vertical wells at different positions (the horizontal position of the wells is given on the right-hand side of the figure). The shape of the temperature profile depends on the direction of the ground water flow. The recharge area (zone I) is characterized by a decrease of the temperature with respect to the reference temperature gradient while the opposite situation arises in the discharge area (zone II). The reference temperature profile corresponds to the boundary between the grey and white areas. The names of the vertical wells are derived from their position (e.g. W35 means that the well is located at 3500 m from the beginning of the profile).

As explained in Section 2, the self-potential anomalies recorded at the ground surface of the Earth and the temperature data recorded in boreholes represent useful and complementary signatures of the flow of the ground water. In the present case, the self-potential profile computed at the ground surface can be subdivided into two anomalies. A positive anomaly (with respect to the value of the potential at the reference electrode) that is associated with the upflow of water in the discharge area and a negative anomaly associated with the recharge area (Figs 2b and 3). Concerning the temperature anomalies, the recharge area is clearly associated, at depth, with a temperature gradient below the mean geothermal gradient (Fig. 4). The opposite occurs for the discharge area (Fig. 4).

We analyse now the sensitivity of the self-potential and thermal signatures to a variation of the material properties of the system. Two stations are monitored. One is located in the recharge area and the second in the discharge area.

3.2 Influence of the permeability

We first investigate the influence of the hydraulic transmissivity of the fault zones upon the two self-potential anomalies. The hydraulic transmissivity is equal to the permeability time the thickness of the fault. In the following, we keep the thickness of the faults as constant and we will only discuss their intrinsic permeability. In the discharge area, Fig. 5(a) shows that the magnitude of the self-potential anomaly is inversely proportional to the permeability. This is easily explained by the fact that in Darcy's law, the hydraulic head gradient varies inversely with permeability when the flux is imposed. The volumetric charge density is also dependent on the permeability of the material (see Fig. 1).

For the recharge area, the situation is a bit more complex to interpret. Indeed, two behaviours can be observed depending on the value of the permeability with respect to a critical permeability value that is equal to 10^{-14} m^2. This is explained by the fact that the flow pattern, in the recharge area, is strongly influenced by the permeability ratio between the permeability of the fault zone and the permeability of the surrounding material. Consequently, the critical permeability discussed above is just the permeability of the material in which the fault zone is embedded. When the permeability of the fault zone is smaller than the permeability of the surrounding material, the flow pattern is more horizontal, generating an horizontal electrostatic dipole with a negative pole close to the fault zone. This explains the negative self-potential anomaly observed near the fault in this situation. When the fault is more permeable than the surrounding sediment, the fault is a permeable pathway and the strength of the self-potential anomaly is inversely proportional to the permeability of the fault zone. In this case, the self-potential anomaly in the recharge area is not too much influenced by the permeability of the sediments surrounding the fault because of the boundary conditions imposed to the fault at the top surface of the system. This situation corresponds to a forced hydrogeological regime.

The influence of the permeability upon the temperature profiles is exactly the opposite of the influence of the permeability upon the self-potential signals. Fig. 5(b) shows that when the permeability increases, the heat flow increases proportionally to it. As is the case of the self-potential anomaly, the temperature anomaly depends on the ratio of the permeability of the fault to the permeability of the surrounding sediment. In the case where the permeability of the fault is smaller than the permeability of the surrounding sediment, the flow pattern does not create a thermal anomaly because the flow is mainly horizontal (this case corresponds to an annihilator for

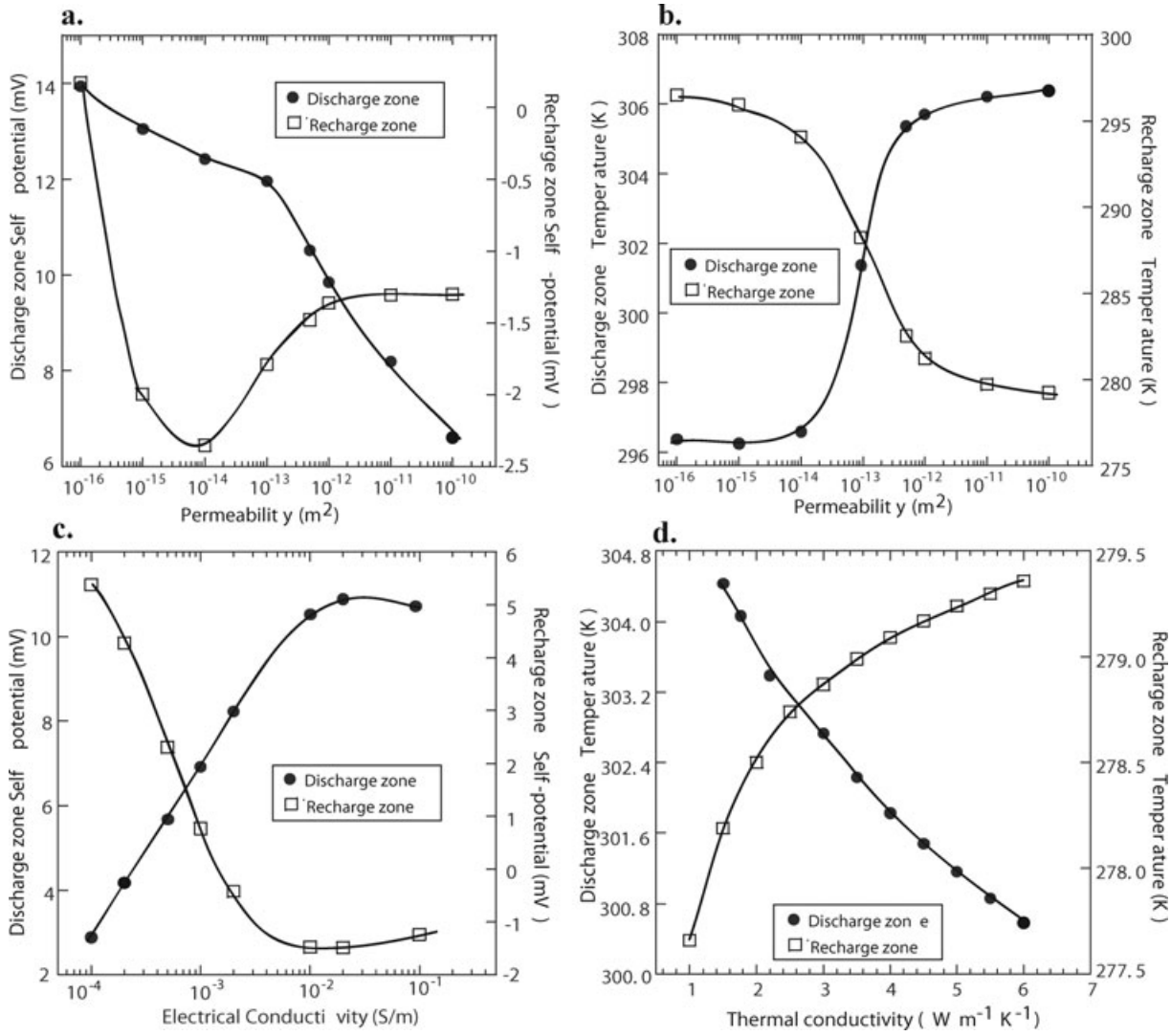

Figure 5. Sensitivity analysis in the recharge and discharge areas. (a) Influence of the permeability upon the strength of the self-potential anomaly at the ground surface. (b) Effect of the permeability on the variations of the temperature profile versus depth. (c) Influence of the electrical resistivity upon the strength of the self-potential anomaly at the ground surface. (d) Sensitivity analysis of the temperature profile versus depth. The lines are guides to the eyes.

the thermal problem). As faults can act as permeability barriers, conduits or both together, both cases can exist in nature.

3.3 Influence of the electrical conductivity

Electrical conductivity is a key-parameter influencing the distribution of the self-potential data, both in term of polarity and strength. Our sensitivity analysis (Fig. 5c) reveals that the strength of the two self-potential anomalies (for the recharge and discharge areas) increases with the increase of the electrical conductivity of the fault zones. If the conductivity ratio between the conductivity of the fault zone and the conductivity of the surrounding material is very strong, the polarity of the self-potential anomalies can also changed because of the influence of the secondary sources that can be more important than the primary sources associated with the electrokinetic conversion of the ground water flow. However, the effect of resistivity contrast upon the signature the self potential signals depends on the distance between the primary (electrokinetic) sources and the area where there is a drop in the electrical resistivity It is also important to note, for practical applications, that electrical conductivity can be obtained independently in the field using electrical impedance tomography, low-frequency electromagnetic methods, or borehole data to reconstruct the conductivity of each units including the effect of the salinity of the pore water, the cation exchange capacity, and the temperature.

3.4 Influence of the thermal conductivity

The distribution of the thermal conductivity controls the distribution of the temperature. Fig. 5(d) reveals that the temperature anomalies created by a convective heat flow are better observed when the thermal conductivity is high. However, the domain of variation of the thermal conductivity is relatively small (less than one order of magnitude) by comparison with the domains of variation of permeability and electrical conductivity. Therefore, the influence of the heterogeneity of the thermal conductivity is less important. Consequently, for a given formation, the gradient of the temperature with depth depends mainly on the heat flux at the bottom boundary

and the value of the thermal conductivity of the formation according to the following relationship,

$$g_{\mathrm{G}} \equiv \frac{\partial T}{\partial z} = \frac{q_{\mathrm{G}}}{\lambda}, \tag{4}$$

where g_{G} is the geothermal gradient (in $^{\circ}$C m^{-1}) and q_G is the heat flux (in W m^{-2}). It follows that the isotherms are closer in the region of low thermal conductivity. The heat flux remains roughly the same through all the formations, but distinct thermal conductivities modify locally the temperature gradient.

4 STOCHASTIC JOINT INVERSION

4.1 Description of the algorithm

We use below a Bayesian approach to estimate the material properties $\mathbf{m} = (\mathbf{m}_\sigma, \mathbf{m}_{\mathrm{k}}, \mathbf{m}_\lambda)$ from self-potential and temperature data where $\mathbf{m}_\sigma$ refers to the log of the electrical conductivity distribution, $\mathbf{m}_{\mathrm{k}}$ to the log of the permeability distribution, and $\mathbf{m}_\lambda$ to the log of the thermal conductivity distribution. The Bayesian solution to an inverse problem is based on combining the information coming from the geophysical data with some prior knowledge. The Bayesian analysis considers both the data vector **d** and the model parameters **m** of a model M as random variables. Several geometrical or petrophysical models M are possible to explain the data. Random variables are characterized with distributions and we assume that all distributions have density functions (Gelman *et al.* 2004; Tarantola 2005).

The objective of inverse modelling is to update the information on **m**, assuming a petrophysical model or a geometrical model M, given the data **d** and prior information regarding **m**. The prior information can come from independent observations and petrophysical relationships. In a probabilistic framework, the inverse problem corresponds to maximize the conditional probability density of occurring m of M given the data vector **d**. We note $P_0(\mathbf{m}|\mathrm{M})$. the prior probability density or belief of parameters **m** of model M and $P(\mathbf{d}|\mathbf{m},M)$. represents the likelihood corresponding to the data for fixed **m** and M. The *a posteriori* probability density $\pi(\mathbf{m}|\mathbf{d})$of the model parameters **m** given the data **d** is obtained using Bayes formula

$$\pi(\mathbf{m}|\mathbf{d},M) = \frac{P(\mathbf{d}|\mathbf{m},M)P_0(\mathbf{m}|M)}{P(\mathbf{d}|M)}, \tag{5}$$

where $P(\mathbf{d}|M)$. is a normalizing term known as evidence,

$$P(\mathbf{d}|M) = \int P_0(\mathbf{m}|M)P(\mathbf{d}|\mathbf{m},M)\mathrm{d}\mathbf{m}. \tag{6}$$

In the following, we assume that the model M is certain (For example, we know the position of the sedimentary layers and faults from other geophysical datasets and borehole or geological information and the relationship between the charge density and the permeability is considered to be deterministic.). Therefore, we drop from now the term M from eq. (5). The *a posteriori* probability density $\pi(\mathbf{m}|\mathbf{d})$of the model parameters **m** given the data **d** is written as

$$\pi(\mathbf{m}|\mathbf{d}) \propto P(\mathbf{d}|\mathbf{m})P_0(\mathbf{m}). \tag{7}$$

The Bayesian solution of the inverse problem is the whole posterior probability distribution of the material properties. An estimate of the unknown parameters can be computed, for example, as the expectation value with respect to the posterior distribution (i.e. as the posterior mean value) or as the maximum posterior value. The likelihood function used to assess for the quality of a model **m** can be considered to be Gaussian distributed

$$P(\mathbf{d}|\mathbf{m}) = \frac{1}{[(2\pi)^N \det \boldsymbol{C}_{\boldsymbol{d}}]^{1/2}} \exp\left\{-\frac{1}{2}[g(\mathbf{m}) - d]^T \boldsymbol{C}_{\boldsymbol{d}}^{-1}[g(\mathbf{m}) - \mathbf{d}]\right\} \tag{8}$$

$$\mathbf{d} = (\mathbf{d}_{\mathrm{sp}}, \mathbf{d}_{\mathrm{T}})^T, \tag{9}$$

where $g(\mathbf{m})$ is the forward modelling operator for the thermohydroelectrical problem. It connects the generation of a self-potential anomaly and a temperature anomaly to a variation of the material properties of the ground, **d** is a N-vector of the observed surface self potential data $\mathbf{d}_{\mathrm{sp}}$ and temperature data $\mathbf{d}_{\mathrm{T}}$ 'measured' in boreholes if a joint inversion is performed or just $\mathbf{d}_{\mathrm{sp}}$ or $\mathbf{d}_{\mathrm{T}}$ if only the self-potential or temperature data are considered alone. The $(N\times N)$-covariance matrix $\boldsymbol{C}_{\boldsymbol{d}}$ is a diagonal matrix written as,

$$\boldsymbol{C}_{\boldsymbol{d}} = \begin{bmatrix} \sigma_{\mathrm{sp}}^2 & 0 \\ 0 & \sigma_T^2 \end{bmatrix}, \tag{10}$$

where σ_{sp} and σ_T are determined from the standard deviations on the self-potential and temperature measurements. The measurements errors for the self-potential and temperature data are usually uncorrelated and Gaussian. The prior probability distribution, if available, is also taken Gaussian

$$P_0(\mathbf{m}) = \frac{1}{[(2\pi)^M \det \boldsymbol{C}_{\boldsymbol{m}}]^{1/2}} \exp\left[-\frac{1}{2}(\mathbf{m} - \mathbf{m}_{\mathrm{prior}})^T \boldsymbol{C}_{\boldsymbol{m}}^{-1}(\mathbf{m} - \mathbf{m}_{\mathrm{prior}})\right], \tag{11}$$

where $\boldsymbol{m}_{\mathrm{prior}}$ is the prior value of the model parameters for each unit and $\boldsymbol{C}_{\boldsymbol{m}}$ is the model diagonal covariance matrix incorporating the uncertainties related of the prior model of material properties.

The problem is to explore the *a posteriori* probability density $\pi(\mathbf{m}|\mathbf{d})$ expressed by eq. (7). MCMC algorithms are well suited for Bayesian inference problems of this type. MCMC algorithms consist of random walks where different states (i.e. different values of a model vector) are visited and where the choice of the next state depends only on the value of the current state (Gelman *et al.* 1996; Sen & Stoffa 1996; Mosegaard & Tarantola 1995; Malinverno & Torres-Verdin 2000; Malinverno 2002; Gelman *et al.* 2004). After an initial period in which the random walker moves towards the highest *a posteriori* probability regions, the chain returns a number of model vectors sampling the *a posteriori* probability density $\pi(\mathbf{m}|\mathbf{d})$. The characteristic of the probability density $\pi(\mathbf{m}|\mathbf{d})$, like the mean and the standard deviation can be therefore easily determined. Memory mechanism of the MCMC algorithms (that makes the chain staying in the high *a posteriori* probability regions of the model space) are responsible for a greater efficiency of the algorithm in comparison with the Monte Carlo methods for which the models are independently chosen and tested against the observations (Sternberg 1979).

To improve the performance of the standard Metropolis–Hasting algorithm, Haario *et al.* (2001) introduced recently an algorithm called the AMA to find the optimal proposal distribution. This algorithm is based on the traditional Metropolis algorithm with a symmetric Gaussian proposal distribution centred at the current model $\mathbf{m}^i$ and with the covariance $\boldsymbol{C}^i$ that changes during the sampling in such a way that the sampling efficiency increases

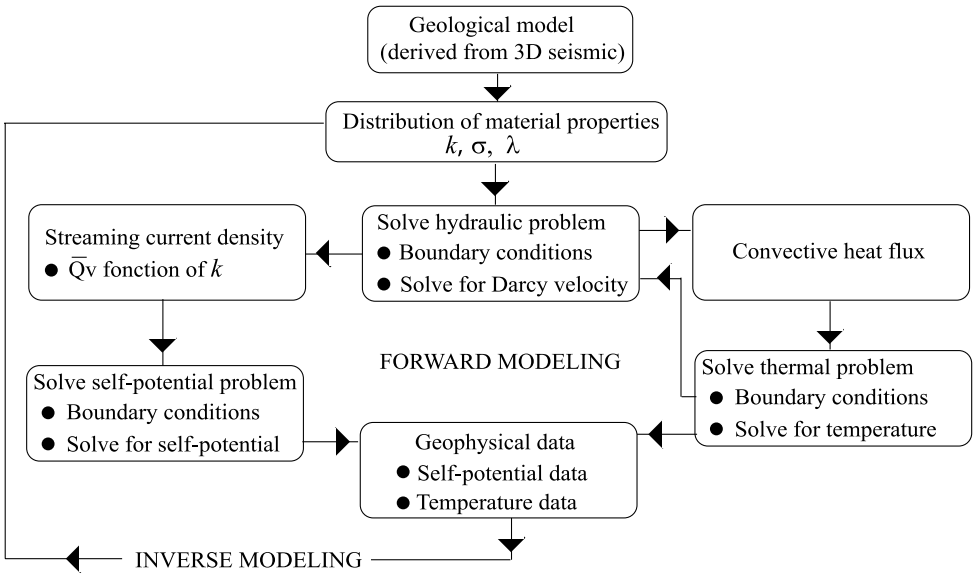

Figure 6. Sketch of the methodology used to jointly invert the self-potential and temperature data associated with the flow of ground water. The inversion of the two types of data yields values of the petrophysical properties (permeability and/or thermal and electrical conductivities) from self-potential measurements at the ground surface and temperature measurements in a set of boreholes.

over time (Haario *et al.* 2001, 2004). It can be shown that the AMA algorithm, though not Markovian, simulates correctly the target distribution. An important advantage of the AMA algorithm is that the rapid start of the adaptation of the algorithm ensures that the search becomes more effective at an early stage of the simulation. This diminishes the number of function evaluations needed. Let us assume that we have sampled the states ($\mathbf{m}^{\circ}, \ldots, \mathbf{m}^{\mathrm{i}-1}$) where $\mathbf{m}^{\circ}$ corresponds to the initial state. Then a candidate point $\mathbf{m}'$ is sampled from the Gaussian proposal distribution q with mean point at the present point $\mathbf{m}^{\mathrm{i}-1}$ and with the covariance

$$\boldsymbol{C}^{\boldsymbol{i}} = \begin{cases} \boldsymbol{C}^{\mathbf{0}} & \text{if } \mathrm{i} \leq \mathrm{n}_0 \\ s_n \boldsymbol{K}^{\boldsymbol{i}} + s_n \varepsilon \boldsymbol{I}_{\boldsymbol{n}} & \text{if } \mathrm{i} > \mathrm{n}_0 \end{cases}, \tag{12}$$

where $\boldsymbol{I}_{\boldsymbol{n}}$ denotes the n-dimensional identity matrix, $\mathbf{K}^{\mathrm{i}} = \mathrm{Cov}(\mathbf{m}^{\circ}, \ldots, \mathbf{m}^{\mathrm{i}-1})$ is the regularization factor (a small positive number that prevents the covariance matrix from becoming singular), $\mathbf{C}^{\circ}$ is the initial covariance matrix that is strictly positive (note that the AMA algorithm is not too sensitive to the actual values of $\mathbf{C}^{\circ}$), $s_n = (2.4)^2/n$ is a parameter that depends only on the dimension of the vector $\mathbf{m} \in \Re^{\boldsymbol{n}}$ (Haario *et al.* 2001). According to Gelman *et al.* (1996), this choice of s_n yields an optimal acceptance in the case of a Gaussian target distribution and a Gaussian proposal distribution. The candidate point $\mathbf{m}'$ is accepted with the acceptance probability

$$\alpha(\mathbf{m}^{i-1}; \mathbf{m}') = \min\left[1, \frac{\pi(\mathbf{m}'|\mathbf{d})}{\pi(\mathbf{m}^{i-1}|\mathbf{d})}\right]. \tag{13}$$

If the candidate point is accepted, we consider that $\mathbf{m}^{\mathrm{i}} = \mathbf{m}'$, otherwise we choose $\mathbf{m}^{\mathrm{i}} = \mathbf{m}^{\mathrm{i}-1}$.

The AMA algorithm was written in a MATLAB routine. The flowchart used to solve the forward and inverse problems is summarized in Fig. 6.

4.2 Results

To see the advantage of performing a joint inversion of the temperature and self-potential data, we first start by inverting the self-potential data and the temperature data separately. We used the AMA sampler with 10 000 iterations using the temperature and self-potential data together (both the thermal conductivity and electrical conductivity distributions are unknown and also determined from the algorithm). In Fig. 7(a), we show that the value of the thermal conductivity of each unit inverted from the temperature data is quite good for all geological units. Fig. 7(b) shows the inversion of the electrical conductivity of each unit when only the self-potential data are used. In the case where only the temperature data are used, Fig. 8(c) demonstrates that the inverted permeabilities are not well reproduced by the algorithm. This result can be easily explained from the underlying physics as the temperature distribution depends only on the vertical component of the Darcy velocity. In other words, because the temperature distribution is not sensitive to the horizontal component of the Darcy velocity, the inversion of the temperature data alone yields the poor result shown by Fig. 8(c) for the permeability.

Fig. 7(b) shows a comparison between the inverted electrical conductivities of each unit and their 'true' values using the self-potential data. Interestingly, self-potential can be used to invert grossly the resistivity value of each unit but the outputs of such an inversion remains rough, especially for the deeper formations. Only the resistivity of the shallow formations and the resistivity of the faults are well reproduced. After few kilometres, the effect of secondary sources does not influence the self-potential distribution at the ground surface.

In Figs 8(a) and (b), we show that the inversion of the permeability is relatively well reproduced by considering the self-potential alone except for the permeability of the basement. This is logical if we consider that the permeability of the basement can take a wide range of low values without affecting the self-potential distribution at the ground surface. The knowledge of the electrical conductivity distribution does not really help the algorithm to reach a better result but the results of the inversion are better than by taking the temperature alone (compare Figs 8a–c).

Fig. 8(d) shows that the joint inversion of the temperature and self-potential data together yields the best estimates of the permeability of each geological unit (compare with Figs 8a–c). Therefore, temperature data in a set of boreholes and self-potential data

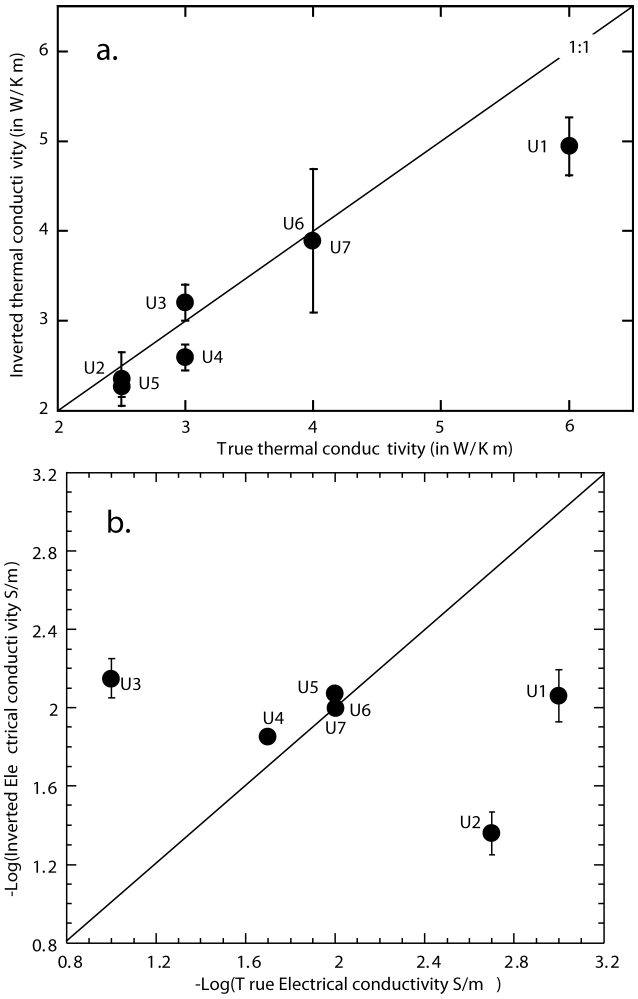

Figure 7. Comparison between inverted and true material properties. (a) Comparison of the inverted thermal conductivity for the different geological units with the true thermal conductivity data. The dots correspond to the mean of the posterior probability distribution sampled with the MCMC algorithm. Only the temperature data are inverted here. (b) The outputs of the inversion are the thermal conductivity and the permeability of each geological unit. Comparison of the inverted electrical conductivity for the different geological units with the true electrical conductivity data. Only the self-potential data are inverted here. Only the shallow formations (U4 and U5) and the two faults (U6 and U7) are well resolved.

are very complementary information to determine the permeability distribution of geological structures.

5 APPLICATION TO CERRO PRIETO

The Cerro Prieto geothermal field is located in the alluvial plain of the Mexicali Valley, northern Baja California, Mexico, at about 35 km southeast of the city of Mexicali (Figs 9a and b). Cerro Prieto was extensively studied and drilled (Fig. 9c) through an international program of collaborative investigations, in the seventies, between the Comision Federal de Electricidad (Mexico) and the Dept. of Energy (USA). It is a suitable target to perform a test of our joint inversion algorithm because it comprises both surface self-potential data and borehole temperatures.

The geological description of this geothermal field can be found in de La Peña & Puente (1979) and the hydrogeology in Lippmann & Bodvarsson (1982, 1983). The available information have been summarized recently by Jardani *et al.* (2008). The Cerro Prieto geothermal field can be grossly divided into three main lithostratigraphic units (de La Peña & Puente 1979) (Fig. 10). The first unit is made of unconsolidated and semi-consolidated continental deltaic sediments of Quaternary age. These sediments show repeated sequences of clays, silts, sands, and gravels and therefore they are quite hydraulically conductive and characterized by low electrical resistivities.

The second unit is composed by consolidated continental deltaic sediments of Tertiary age. These sediments are composed of alternating shales, siltstones, and sandstones presenting lenticular bedding. This implies that the permeability of this unit is anisotropic. The sandstones are fine-grained, usually well-sorted, varying between graywackes and arkoses (de La Peña & Puente 1979; Lyons & van de Kamp 1980). This formation is discordant on the granitic and metasedimentary Upper Cretaceous basement. This basement has suffered tectonic uplift and falls. It is electrically resistive (Wilt & Goldstein 1981). A simplified geological cross-section in the central part of profile EE' (see position in Fig. 9c) is shown in Fig. 10.

A map of the self-potential anomalies measured over the Cerro Prieto geothermal field has been presented by Fitterman & Corwin (1982). This map covers an area of $\approx$300 km^2. A 2-D profile is shown on Fig. 11(a). The self-potential anomaly of Cerro Prieto is definitely 3-D (*cf*. Fitterman & Corwin 1982; Jardani *et al* 2008), but the inversion done below will be performed in 2-D. The geometry of the hydrogeological system for the numerical simulations is sketched in Fig. 11(b) and is taken from Manon *et al.* (1977) and Wilt & Goldstein (1981). In our nomenclature, Unit U1 corresponds to the granitic and metasedimentary Upper Cretaceous basement while Unit U2 corresponds to a zone characterized by intense hydrothermal alteration (Wilt & Goldstein 1981). In the interpretation of dipole–dipole resistivity data made by Wilt & Goldstein (1981), Unit U3 appears as a thin eastward-dipping conductive body contrasting sharply with the surrounding more resistive formations (Units U2 and U4). Unit 7 corresponds to a zone of hot water discharge. Units U4, U5, and U6 are characterized by high clay contents. They are however more resistive than the rocks westward by a factor of 5 (Wilt & Goldstein 1981 and Table 2). According to Lyons & Van de Kamp (1980), this increase in resistivity is due to the transition from brackish pore water to fresher ground waters associated with a recharge of the system in this part of the EE' profile. Some recharge also takes place in units U9 and U10 (see Lippman & Bodvarsson 1982, 1983).

We assume that the resistivity distribution is known (this is actually the case along profile EE' as discussed by Jardani *et al.* 2008). Because the thermal conductivity of the encountered lithologies is fairly well known, we also consider that their values are known. The resistivity and thermal conductivity values for each of the 10 formations of Fig. 11(b) are summarized in Table 2. The unknowns of the inverse problem are the horizontal and vertical effective permeabilities of each geological unit and the constraints are the self-potential data measured at the ground surface (see Fig. 11(a) and the temperature profile observed in the nine wells of Fig. 11b). The temperature data used for the inversion are displayed in Fig. 12.

The forward problem is solved with the following boundary conditions, which are taken from Lippman & Bodvarsson (1983) in agreement with field observation of the recharge areas. For the flow problem, we impose at the top surface of the system a hydraulic pressure of 7.62×10^6 Pa for x comprises from 11.5 to 15.5 km. On the left-hand side of the system ($x = 0$ km) and for 0 km $< z <$0.550 km, we impose an excess fluid pressure of 7×10^6 Pa

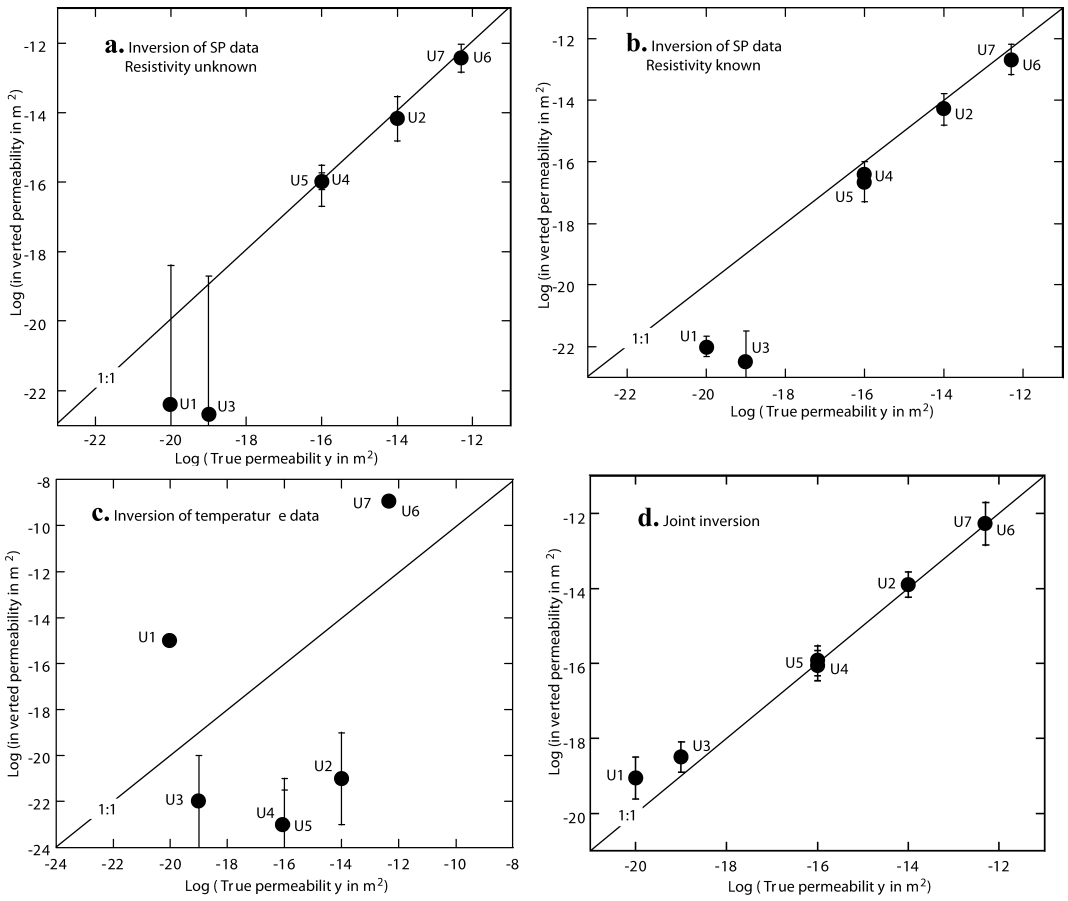

Figure 8. Comparison between the inverted permeability and the true permeability. The dots represent the mean of the posterior probability distributions. (a) Result of the inversion of the self-potential data alone. The resistivity is unknown and is also obtained as a result of the inversion. (b) Result of the inversion of the self-potential data alone with the electrical resistivity assumed to be perfectly known. (c) Result of the inversion of the temperature data alone. (d) Result of the joint inversion of the self-potential and temperature data. The joint inversion provides clearly the most reliable estimates of the permeability of each unit.

and for 0.55 km $< z <$ 2 km, we impose a hydraulic flux of 8×10^{-9} m s^{-1}. On the right-hand side of the system ($x = 15.5$ km), we impose a hydraulic pressure of 7.5×10^6 Pa for 3.00 km $< z <$ 4.07 km. All the other boundaries are impervious. We point out that while the hydraulic boundary conditions are quite well constrained for the Cerro Prieto geothermal field. This may not be the case elsewhere. In the case where this would not be the case, the boundary conditions should be inverted together with the material properties of each unit.

For the modelling of the heat flow, the temperature is fixed using different types of constraints among, which is the temperature distribution in a number of geothermal wells. We use the following boundary conditions. At the upper boundary of the model we use $T = 50$ °C for x comprised between 0 and 6.9 km to account for the discharge of hot water in this area (see Fig. 9c). For 6.9 km $< x <$ 15.5 km, $T = 30$ °C. On the left-hand side of the model ($x = 0$), for $0 < z <$ 0.55 km, we impose $T = 220$ °C because of the observed shallow horizontal flow of hot water in the U7 formation. For 0.55 km $< z <$ 2 km ($x = 0$), we use $T = 150$ °C. For 2 km $< z <$ 3 km, T is fixed at 220 °C. On the right-hand side of the system (15.5 km), and for 2.6 km $< z <$ 4.1 km, we impose $T = 300$ °C. Along the bottom boundary of the system, we impose $T = 640$ °C to reproduce the mean geothermal gradient along the profile. All the other boundaries are insulating boundaries.

For the self-potential signals, we used insulating boundary conditions at the top and bottom surfaces of the system and the boundary condition $\varphi = 0$ on the side boundaries using a padded mesh to avoid the effect of this boundary condition over the investigated area.

The inverse problem is performed by performing 5000 realizations using the AMA sampler. The optimized vertical and horizontal permeabilities of each unit are listed in Table 3 with the standard deviation determined from the last 1000 iterations of the MCMC sampler. These optimized values yield the flow model shown in Fig. 13(c) with the fit of the self-potential and temperature data shown in Figs 13(a) and (b), respectively.

Regarding the values of the permeabilities, we point out that we did not use any prior information to constrain their values. The permeability of the basement unit U1 is found to be very low as expected (the mean value is 10^{-18} m^2). The optimized permeability of Unit U3, that contains the transmissive fault, is found to be quite high (mean of 10^{-13} m^2). The mean value we found (10^{-13} m^2) is in excellent agreement with the value used by Lippmann & Bodvarsson (1982, their table 1) for the isotropic fault material (5×10^{-14} m^2). U2 that is known to be hydrothermalized is found to have a lower permeability ($\sim 10^{-14}$ m^2). The permeabilities of formations U4 and U5 are lower by one order of magnitude (10^{-15} m^2) in agreement with the higher clay-content of these formations. Formation U7 has very high horizontal and vertical permeabilities in agreement with field observations. Indeed this formation corresponds to a discharge area of the hydrothermal system and horizontal shallow flow of hot water as discussed above (see Fig. 9c and Jardani *et al.*

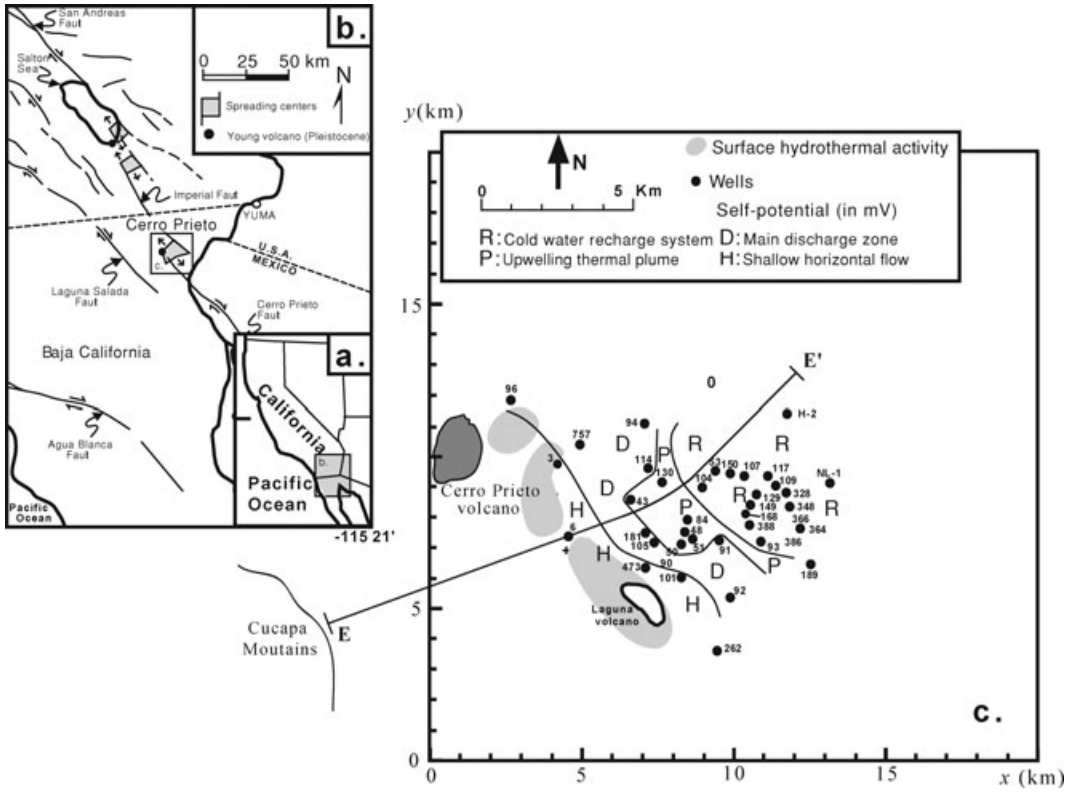

Figure 9. Localization of the investigated profile EE' in the Cerro Prieto geothermal field. (a and b) The Cerro Prieto geothermal field is located in Baja California (Mexico), between the southeast end of the Imperial Fault and the northern end of the Cerro Prieto Fault. (c) Position of the profile EE' with respect to the recharge and discharge areas of the hydrothermal systems. This profile has been chosen because it is normal to the main geothermal features of the system.

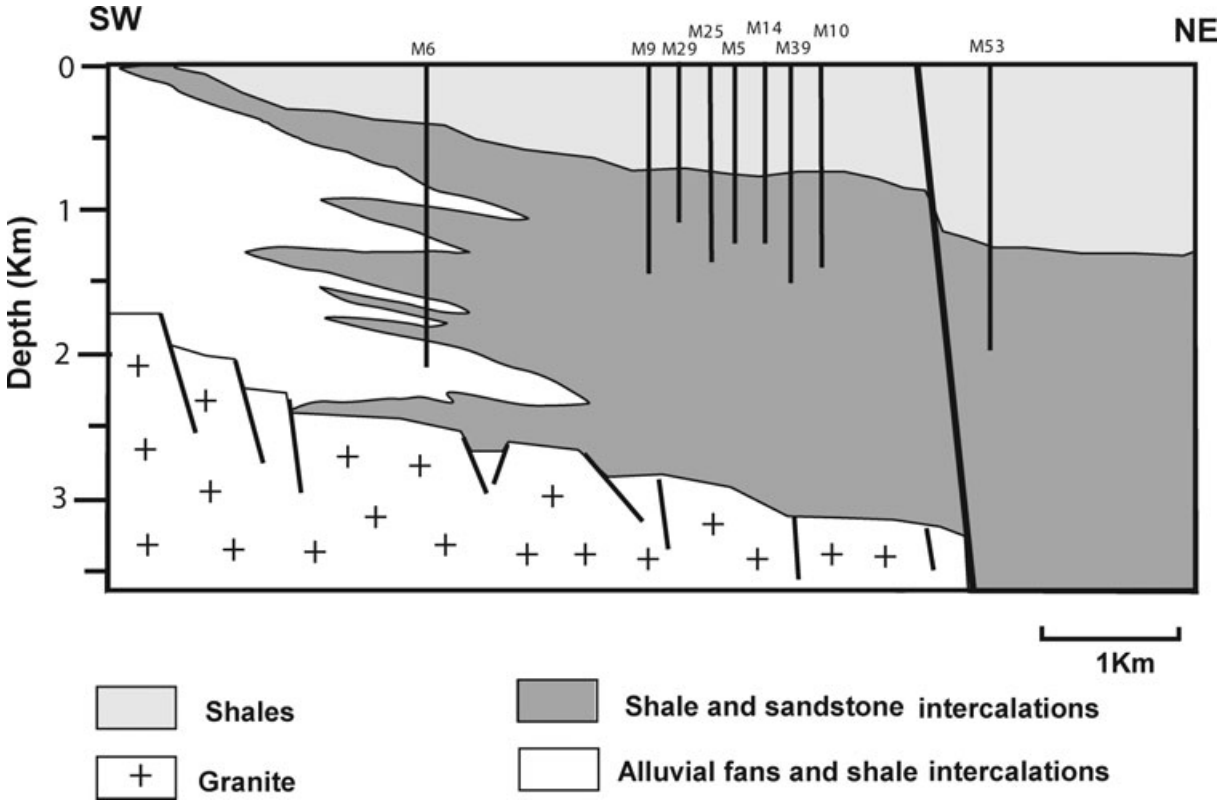

Figure 10. Simplified geological description of the central part of the investigated cross-section EE' in the Cerro-Prieto geothermal field with the position of the geothermal wells used for the temperature. The position of wells M6 and M53 can be found in Fig. 13(c) (modified from Manon *et al.* 1977).

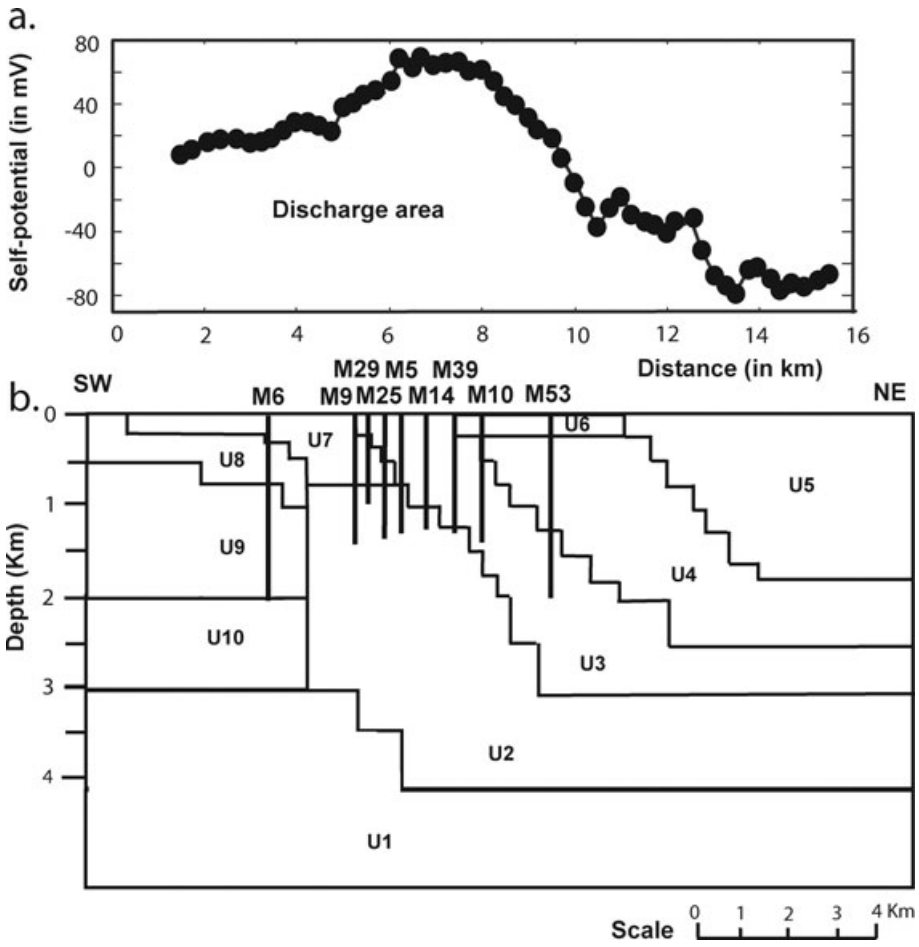

Figure 11. Self-potential data and simplified geological model used for the inversion. The model comprises 10 geological units labelled U1 to U10. (a) The self-potential data are taken from Fitterman & Corwin (1982). (b) The hydrogeological model is taken from the resistivity profile EE' discussed by Wilt & Goldstein (1981). The value of the resistivity of the geological units are taken from Wilt & Goldstein (1981) (their fig. 3) and are reported in Table 2. The self-potential anomaly points out that the flow occurs mainly in Units U2 and U3 (see Corwin *et al.* 1979).

Table 2. Material properties (electrical resistivity and thermal conductivities) used for the model of Cerro Prieto.

Unit	ρ^a (in ohm m)	λ^b (in W m^{-1} K^{-1})
U1	300	1.5
U2	4.0	3.0
U3	1.5	3.0
U4	5.0	3.0
U5	8.5	2.0
U6	2.2	3.0
U7	0.6	2.0
U8	3.5	2.5
U9	1.2	2.5
U10	2.0	3.0

[a]The resistivity data are from Wilt & Goldstein (1981).
[b]The resistivity data are from Lippman & Bodvarsson (1982).

2008). Units U8, U9 and U10 have a high anisotropy of permeability with a very high horizontal permeability. This is consistent with the known lithology of these formations (see Fig. 10) because of the interbedding of shale and sand geological formations. For the formations U8 and U9, Lippmann & Bodvarsson (1982, their table 1) used an horizontal permeability of 10^{-13} m^2 and a vertical permeability of 10^{-14} m^2 in close agreement with the optimized values reported in Table 3 using the self-potential and temperature data as constraints.

We can therefore conclude that the parametric inversion developed in the present paper and based on the joint inversion of temperature and self-potential data yields correct estimates of the large-scale permeability of these formations.

6 CONCLUDING STATEMENTS

We have developed a joint inversion algorithm for self-potential and temperature data. Because self-potential data are usually measured at the ground surface while temperature data are measured in boreholes, these two datasets offer complementary information for a joint inversion problem. An AMA is used to perform this task. The application of this algorithm to a synthetic 2-D case shows the advantage in using the joint inversion approach by comparison with the results of the inversion of the self-potential or temperature data sets alone. There are two reasons for this improvement. The first one is related to the fact that the support of the information is complementary for both data sets (ground surface and boreholes). The second reason is that the annihilators are usually different for the thermal and the self-potential problems. This algorithm was

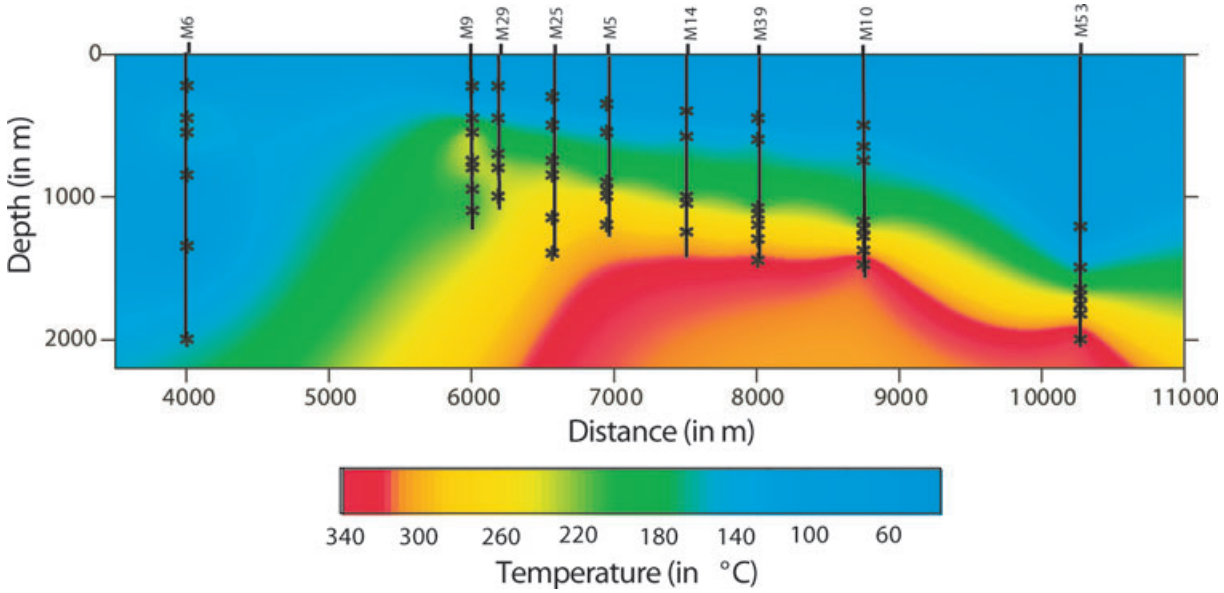

Figure 12. Interpolation of the temperature data in different geothermal wells in the central part of the profile EE'. The stars along the borehole indicate the position of the temperature data used for the inversion.

Table 3. Value of the optimized horizontal and vertical permeability for each unit of the Cerro Prieto geothermal field.

Material	Log (k_x) (k_x in m^2)	Log (k_z) (k_z in m^2)
U1	-18.0 ± 1.8	-18.0 ± 1.8
U2	-14.2 ± 0.5	-15.1 ± 1.5
U3	-13.0 ± 0.8	-15.3 ± 0.8
U4	-15.1 ± 0.3	-15.1 ± 0.3
U5	-15.0 ± 0.5	-14.1 ± 1.5
U6	-15.6 ± 0.3	-17.2 ± 1.0
U7	-13.7 ± 2.1	-14.1 ± 1.2
U8	-13.0 ± 1.8	-15.0 ± 0.5
U9	-12.4 ± 2.1	-13.0 ± 1.0
U10	-14.5 ± 2.1	-16.1 ± 0.68

applied successfully to the self-potential and temperature data of the Cerro Prieto geothermal field in Baja California. The permeabilities resulting from the inversion are consistent with independent hydrogeological studies based on test production.

ACKNOWLEDGMENTS

We thank the US Department of Energy, Grant N° DE-FG36–08GO018195. We also thank T. Young for his support at the Colorado School of Mines and L. Tenorio for fruitful discussions. We thank the two Associate Editors of a first version of this manuscript (M. Everett and O. Ritter) and two anonymous referees for their helpful reviews.

REFERENCES

Andrews, C.B. & Anderson, M.P., 1979. Thermal alteration of groundwater caused by seepage from a cooling lake, *Water Resour. Res.,* **15**(3), 595–602.

Arora, T., Revil, A., Linde, N. & Castermant, J., 2007. Non-intrusive determination of the redox potential of contaminant plumes using the self-potential method, *J. Contam. Hydrol.,* **92**(3–4), 274–292.

Bernabé, Y. & Revil, A., 1995. Pore-scale heterogeneity, energy dissipation and the transport properties of rocks, *Geophys. Res. Lett.,* **22**(12), 1529–1552.

Bishop, B.P. & Bird, D.K., 1987. Variation in sericite compositions from fracture zones within the Coso hot springs geothermal system, *Geochim. Cosmochim. Acta,* **51,** 1245–1256.

Bolève, A., Revil, A., Janod, F., Mattiuzzo, J.L. & Jardani, A., 2007. Forward modeling and validation of a new formulation to compute self-potential signals associated with ground water flow, *Hydrol. Earth Syst. Sci.,* **11**(5), 1661–1671.

Brace, W., 1977. Permeability from resistivity and pore shape, *J. geophys. Res.,* **82**(23), 3343–3349.

Bredehoeft, J.D. & Papadopulos, I.S., 1965. Rates of vertical ground-water movement estimated from the Earth's thermal profile, *Water Resour. Res.,* **1**(2), 325–328.

Castermant, J., Mendonça, C.A., Revil, A., Trolard, F., Bourrié, G. & Linde, N., 2008. Redox potential distribution inferred from self-potential measurements during the corrosion of a burden metallic body, *Geophys. Prospect.,* **56,** 269–282, doi:10.1111/j.1365-2478.2007.00675.x.

Cheviron, B., Guérin, R., Tabbagh, A. & Bendjoudi, H., 2005. Determining long-term effective groundwater recharge by analyzing vertical soil temperatures profiles at meteorological stations, *Water Resour. Res.,* **41**(9), 12–17.

Corwin, R.F. & Hoover, D.B., 1979. The self-potential method in geothermal exploration, *Geophysics,* **44,** 226–245.

Corwin, R.F., Morrison, H.F., Diaz, S. & Rodriguez, J., 1979. Self-potential studies at the Cerro Prieto geothermal field, in *Proceedings of the First Symposium on the Cerro Prieto Geothermal Field,* Baja California, Mexico, September 20–22, 1978, San Diego, Lawrence Berkeley Lab, Report LBL-7098, pp. 204–210.

Crespy, A., Revil, A., Linde, N., Byrdina, S., Jardani, A., Bolève, A. & Henry, P., 2008. Detection and localization of hydromechanical disturbances in a sandbox using the self-potential method, *J. geophys. Res.,* **113,** B01205, doi:10.1029/2007JB005042.

de la Peña, L.A. & Puente, C.I., 1979. The geothermal field of Cerro Prieto, in *Geology and Geothermics of the Salton Trough,* pp. 20–35, ed. Elders, W.A., Riverside, University of California, Inst. of Geophysics and Planetary Phys., Report UCR/IGPP-79/23.

Fetter, C.W., 1994. *Applied Hydrogeology*. ISBN 0-02-336490-4, Prentice Hall, New Jersey, 691 pp.

Fitterman, D.V. & Corwin, R.F., 1982. Inversion of self-potential data from the Cerro Prieto geothermal field, Mexico, *Geophysics,* **47,** 938–945.

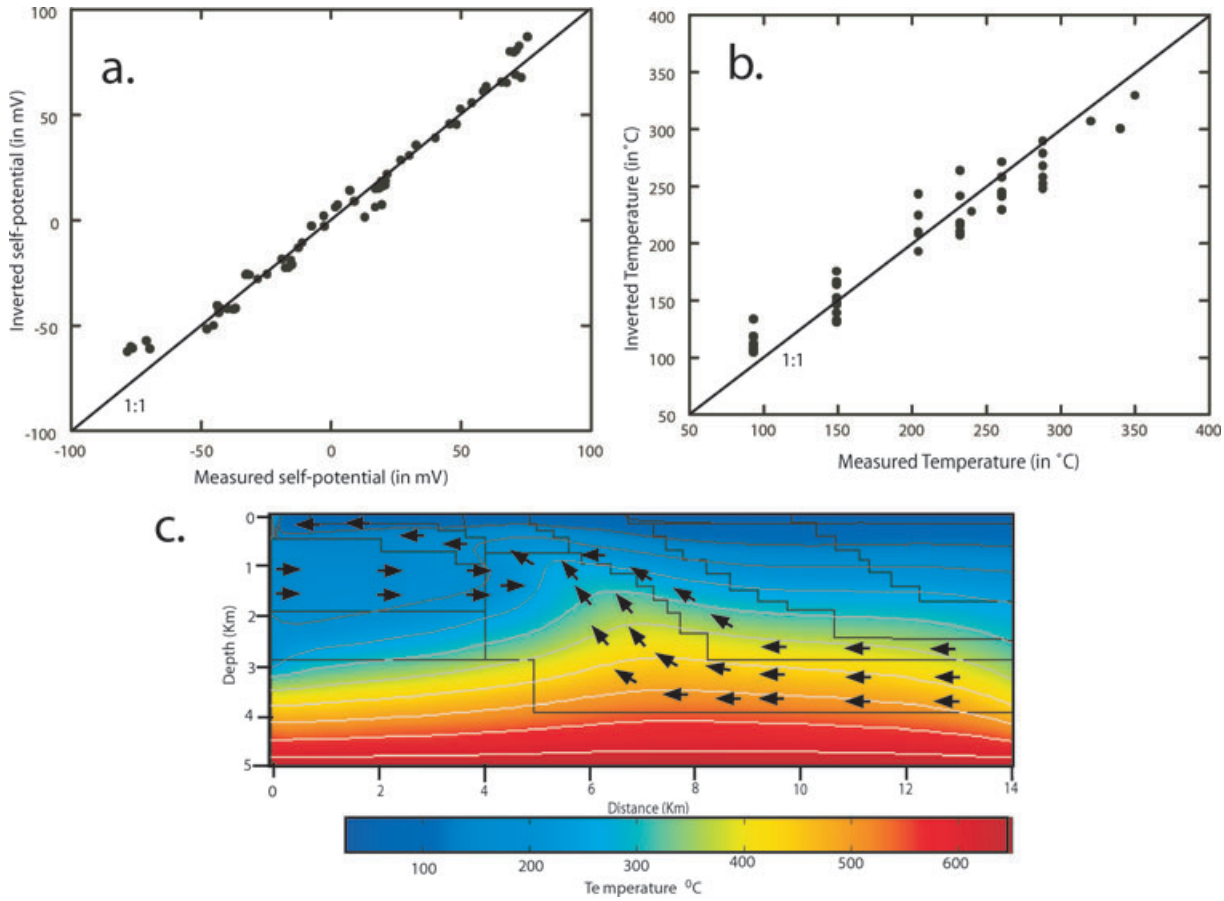

Figure 13. Results of the inversion. (a) Best fit of the self-potential data from Fig. 15(a). (b) Best fit of the temperature data from Fig. 16. (c) Flow pattern associated with the highest posterior probability densities of the permeabilities values of each geological unit. Note the upflow of the hot water in the central part of the system and the horizontal flow in the Western part of the system. The arrows represent the direction of the Darcy velocity with a threshold value of 5×10^{-9} m s^{-1}.

Forster, C. & Smith, L., 1988. Groundwater flow systems in mountainous terrain 2. Controlling factors, *Water Resour. Res.,* **24**(7), 1011–1023.

Friedman, S. & Seaton, N., 1998. Critical Path Analysis of the relationship between permeability and electrical conductivity of three-dimensional pore networks, *Water Resour. Res.,* **34**(7), 1703–1710.

Gelman, A.G., Roberts, G.O. & Gilks, W.R., 1996. *Efficient Metropolis jumping rules, in Bayesian Statistics V,* pp. 599–608, eds Bernardo, J.M. *et al*., Oxford Univ. Press, New York.

Gelman, A.G., Carlin, J.B., Stern, H.S. & Rubin, D.B., 2004. *Bayesian Data Analysis,* 2nd edn, London CRC Press, London.

Haario, H., Saksman, E. & Tamminen, J., 2001. An adaptive Metropolis algorithm, *Bernoulli,* **7,** 223–242.

Haario, H., Laine, M., Lehtinen, M., Saksman, E. & Tamminen J., 2004. MCMC methods for high dimensional inversion in remote sensing, *J. R. Stat. Soc., Ser. B.,* **66,** 591–607.

Jardani, A., Revil, A., Akoa, F., Schmutz, M., Florsch, N. & Dupont J.P., 2006. Least-squares inversion of self-potential (SP) data and application to the shallow flow of the ground water in sinkholes, *Geophys. Res. Lett.,* **33**(19), L19306, doi:10.1029/2006GL027458.

Jardani, A., Revil, A., Bolève, A., Dupont, J.P., Barrash, W. & Malama, B., 2007. Tomography of groundwater flow from self-potential (SP) data, *Geophys. Res. Lett.,* **34,** L24403, doi:10.1029/2007GL031907.

Jardani, A., Revil, A., Bolève, A. & Dupont, J.P., 2008. 3D inversion of self-potential data used to constrain the pattern of ground water flow in geothermal fields, *J. Geophys. Res.,* **113,** B09204, doi:10.1029/2007JB005302.

Jougnot, D., Revil, A. & Leroy, P., 2009. Diffusion of ionic tracers in the Callovo-Oxfordian clay-rock using the Donnan equilibrium model and the electrical formation factor, *Geochem. Cosmochem. Acta,* **73,** 2712–2726.

Jouniaux, L. & Pozzi, J.P., 1995. Streaming potential and permeability of saturated sandstones under triaxal stress–Consequences for electrotelluric anomalies prior to earthquakes, *J. geophys. Res.,* **100**(B6), 10 197–10 209.

Lachassagne, P. & Aubert, M., 1989. Etude des phénomènes de polarisation spontané (PS) enregistrées dans le sol de transferts hydriques verticaux, *Hydrogéologie,* **1,** 7–17.

Leroy, P., Revil, A., Altmann, S. & Tournassat, C., 2007. Modeling the composition of the pore water in a clay-rock geological formation (Callovo-Oxfordian, France), *Geochim. Cosmochim. Acta,* **71**(5), 1087–1097. doi:10.1016/j.gca.2006.11.009.

Leroy, P., Revil, A., Kemna, A., Cosenza, P. & Gorbani, A., 2008. Spectral induced polarization of water-saturated packs of glass beads, *J. Colloid Interface Sci.,* **321**(1), 103–117.

Linde, N., Jougnot, D., Revil, A., Matthaï, S.K., Arora, T., Renard, D. & Doussan, C., 2007. Streaming current generation in two-phase flow conditions, *Geophys. Res. Lett.,* **34**(3), L03306, doi:10.1029/2006GL028878.

Lippmann, M.J. & Bodvarsson, G.S., 1982. *Modeling Studies on Cerro Prieto, Presented at the 4th Symposium on the Cerro Prieto Geothermal Field,* pp. CP–25, Lawrence Berkeley Lab., Guadalajara, Mexico, August 10–12, 1982, Report LBL-14897.

Lippmann, M.J. & Bodvarsson, G.S., 1983. Numerical studies of the heat and mass transport in the Cerro Prieto geothermal field, Mexico, *Water Resour. Res.,* **19,** 753–767.

Lyons, D.J. & van de Kamp, P.C., 1980. *Subsurface Geological and Geophysical Study of the Cerro Prieto Geothermal Field,* Berkeley, Lawrence Berkeley Laboratory, pp. LBL-10540.

Malinverno, A., 2002. Parsimonious Bayesian Markov chain Monte Carlo inversion in a non-linear geophysical problem, *Geophys. J. Int.,* **151,** 675–688.

Malinverno, A. & Torres-Verdin, C., 2000. Bayesian inversion of DC electrical measurements with uncertainties for reservoir monitoring, *Inverse Problems,* **16,** 1343–1356.

Manon, A., Jimenez, M.E., Sanchez, A., Fausto, J.J., Zenizo, C.A. & Mazon, E., 1977. Extensive Geochemical Studies in the Geothermal Field of Cerro Prieto, Mexico, Report, Lawrence Berkeley Laboratory.

Mosegaard, K. & Sambridge, M., 2002. Monte Carlo analysis of inverse problems, *Inverse Problems,* **18,** 29–54.

Mosegaard, K. & Tarantola, A., 1995. Monte Carlo sampling of solutions to inverse problems, *J. geophys. Res.,* **100,** 12 431–12 447.

Pengra, D.B., Li, S.X. & Wong, P.-Z., 1999. Determination of rock properties by low-frequency AC electrokinetics, *J. geophys. Res.,* **104**(B12), 29 485–29 508.

Rath, V., Wolf, A. & Bücker, M., 2006. Joint three-dimensional inversion of coupled groundwater flow and heat transfer based on automatic differentiation: sensitivity calculation, verification, and synthetic examples, *Geophys. J. Int.,* **167**(1), 453–466, doi:10.1111/j.1365-246X.2006.03074.x.

Revil, A., 1999. Ionic diffusivity, electrical conductivity, membrane and thermoelectric potentials in colloids and granular porous media: a unified model, *J. Colloid Interface Sci.,* **212,** 503–522.

Revil, A., 2000. Thermal conductivity of unconsolidated sediments with geophysical applications, *J. geophys. Res.,* **105,** 16 749–16 768.

Revil, A. & Cathles, L.M., 2002. Fluid transport by solitary waves along growing faults: a field example from the South Eugene Island Basin, Gulf of Mexico, *Earth planet. Sci. Lett.,* **202**(2), 321–335. (erratum: Revil, A. & Cathles, L.M., 2002. Fluid transport by solitary waves along growing faults: a field example from the South Eugene Island Basin, Gulf of Mexico, Earth Planet. Sci. Lett., 204(1–2), 321–322.

Revil, A. & Linde, N., 2006. Chemico-electromechanical coupling in microporous media, *J. Colloid Interface Sci.,* **302,** 682–694.

Revil, A. & Pezard, P.A., 1998. Streaming potential anomaly along faults in geothermal areas, *Geophys. Res. Lett.,* **25**(16), 3197–3200.

Revil, A., Schwaeger, H., Cathles, L.M. & Manhardt, P., 1999. Streaming potential in porous media. 2. Theory and application to geothermal systems, *J. geophys. Res.,* **104**(B9), 20 033–20 048.

Revil, A., Ehouarne, L. & Thyreault, E., 2001. Tomography of self-potential anomalies of electrochemical nature, *Geophys. Res. Lett.,* **28**(23), 4363–4366.

Revil, A., Hermitte, D., Spangenberg, E. & Cochémé, J.J., 2002. Electrical properties of zeolitized volcaniclastic materials, *J. geophys. Res.,* **107**(B8), 2168, doi:10.1029/2001JB000599.

Revil, A., Leroy, P. & Titov, K., 2005. Characterization of transport properties of argillaceous sediments. Application to the Callovo-Oxfordian Argillite, *J. geophys. Res.,* **110,** B06202, doi:10.1029/2004JB003442.

Revil, A., Linde, N., Cerepi, A., Jougnot, D., Matthäi, S. & Finsterle, S., 2007. Electrokinetic coupling in unsaturated porous media, *J. Colloid Interface Sci.,* **313**(1), 315–327, doi:10.1016/j.jcis.2007.03.037.

Rizzo, E., Suski, B., Revil, A., Straface, S. & Troisi, S., 2004. Self-potential signals associated with pumping tests experiments, *J. geophys. Res.,* **109,** B10203, doi:10.1029/2004JB003049.

Rozycki, A., Fonticiella, J.M.R. & Cuadra, A., 2006. Detection and evaluation of horizontal fractures in Earth dams using self-potential method, *Eng. Geol.,* **82**(3), 145–153.

Sambridge, M. & Mosegaard, K., 2002. Monte Carlo methods in geophysical inverse problems, *Rev. Geophys.,* **40**(3), 1009, doi:10.1029/2000RG000089.

Sen, M. & Stoffa, P.L., 1996. Global optimization methods in geophysical inversion, *Advances in Exploration Geophysics,* Vol. 4, Elsevier, Amsterdam.

Sheffer, M., 2007. Forward modeling and inversion of streaming potential for the interretation of hydraulic conditions from self-potential data, *PhD thesis*. the University of British Columbia.

Smith, L. & Chapman, D.S., 1983. On the thermal effects of groundwater flow 1. Regional scale systems, *J. geophys. Res.,* **88**(B1), 593–608.

Sternberg, B.K., 1979. Electrical resistivity of the crust in the southern extension of the Canadian shield –layered earth models, *J. geophys. Res.,* **84,** 212–228.

Stoll, J., Bigalke, J. & Grabner, E.W., 1995. Electrochemical modelling of self-potential anomalies, *Surv. Geophys.,* **16,** 107–120.

Suski, B., Revil, A., Titov, K., Konosavsky, P., Dagès, C., Voltz, M. & Huttel, O., 2006. Monitoring of an infiltration experiment using the self-potential method, *Water Resour. Res.,* **42,** W08418, doi:10.1029/2005WR004840.

Tabbagh, A., Bendjoudi, H. & Benderitter, Y., 1999. Determination of recharge in unsaturated soils using temperature monitoring, *Water Resour. Res.,* **35**(8), 2439–2446.

Tarantola, A., 2005. *Inverse Problem Theory. Methods for model parameter estimation,* SIAM, Philadelpha.

Tosha, T., Matsushima, N. & Ishido, T., 2003. Zeta potential measured for an intact granite sample at temperatures to 200°C, *Geophys. Res. Lett.,* **30**(6), 1295.

Wilt, M.J. & Goldstein, N.E., 1981. Results of two years of resistivity monitoring at Cerro Prieto, in *Third Symposium on the Cerro Prieto Geothermal Field,* Baja California, Mexico, March 24–26, 1981, Proceedings/Actas CONF-810399–27, pp. 372–376.